


Pressure-induced switching of electronic nematicity in the iron-based ladder materials $\text{BaFe}_2(\text{S}_{1-x}\text{Se}_x)_3$ ($x = 0-1$)

 Takuya Aoyama^{1,*}, Rinto Nojima¹, Touru Yamauchi², Yoshinori Imai¹ and Kenya Ohgushi¹
¹*Department of Physics, Graduate School of Science, Tohoku University, 6-3 Aramaki-Aoba, Aoba-ku, Sendai, Miyagi 980-8578, Japan*
²*Institute for Solid State Physics, University of Tokyo, Kashiwa, Chiba 277-8581, Japan*
 (Received 13 July 2022; revised 25 July 2023; accepted 25 August 2023; published 12 September 2023)

We examined a pressure dependence of an electronic nematicity in iron-based ladder materials $\text{BaFe}_2(\text{S}_{1-x}\text{Se}_x)_3$ with a quasi-one-dimensional ladder lattice by tracking an anomaly in the resistivity. For $x = 0$, the ferroic nematicity observed at ambient pressure is stabilized by applying pressure up to 2 GPa. For $x = 0.25, 0.60,$ and 1 , the antiferroic nematicity at ambient pressure switches into ferroic nematicity by applying pressures of 0.50–4.0 GPa. We present the electronic phase diagram of $\text{BaFe}_2(\text{S}_{1-x}\text{Se}_x)_3$ in terms of the lattice parameters, and discuss the relationship between the nematicity and bandwidth. We also discuss that the external pressure causes a filling control through the charge transfer from anions to cations in the Se-rich compositions.

 DOI: [10.1103/PhysRevB.108.094507](https://doi.org/10.1103/PhysRevB.108.094507)

I. INTRODUCTION

Electronic nematicity, which is a symmetry breaking of an electronic system, is an important issue in iron-based superconductors [1–8]. In iron-based superconductors with a square lattice, d_{yz} and d_{zx} orbitals are degenerate because of the fourfold rotational symmetry of the crystal structure. This degeneracy is lifted by breaking the fourfold rotational symmetry in an electronic system [9,10]. Breaking the symmetry often induces structural phase transitions through electron-lattice coupling. Analogous to classical liquid crystals, this type of anisotropy in electronic systems is called electronic nematicity [11–13].

Electronic nematicity is also discussed in quasi-one-dimensional ladder compounds BaFe_2S_3 and BaFe_2Se_3 , which show a pressure-induced Mott transition and superconductivity [16–19] [Fig. 1(a)]. Electronic nematicity in BaFe_2S_3 and BaFe_2Se_3 is characterized by a weak anomaly in the electrical resistivity, which occurs far above the Néel temperature (T_N) [20–22]. In $\text{BaFe}_2\text{S}_3/\text{BaFe}_2\text{Se}_3$, the divergence of the electrical resistivity toward lower temperatures is suppressed/enhanced below a certain temperature, as shown in the diamond and triangle symbols in Fig. 1(b). The origin of these anomalies has been studied in detail by analyzing the angle-resolved magnetoresistance effects, elastoresistance, optical conductivity, nonlinear optical effect, and x-ray absorption spectroscopy [15,21–24]. These experimental results can be interpreted using the theoretically proposed two-orbital effective model [25,26] as follows. In BaFe_2S_3 , the d_{zx} orbitals are mainly responsible for the electrical conduction near room temperature, but the $d_{x^2-y^2}$ orbitals with a weaker electron correlation also participate in the electrical conduction below $T_F^* = 180$ K, which suppresses the increase in electrical resistivity [24]. Furthermore, the absence

of anisotropy in the magnetoresistance effect on a leg-rung plane around T_F^* indicates the formation of an almost isotropic electronic state. This phenomenon can be regarded as a ferroic nematicity that is caused by the ordering of the d_{zx} and $d_{x^2-y^2}$ orbitals [Fig. 1(c)]. In BaFe_2Se_3 , the distinct type of nematicity occurs at $T_{AF}^* = 400$ K. The ordered pattern of orbitals involves the antiferroic arrangement of the d_{zx} and $d_{x^2-y^2}$ orbitals [Fig. 1(c)]. In this orbital arrangement, the orbitals are orthogonal between many bonds, which well

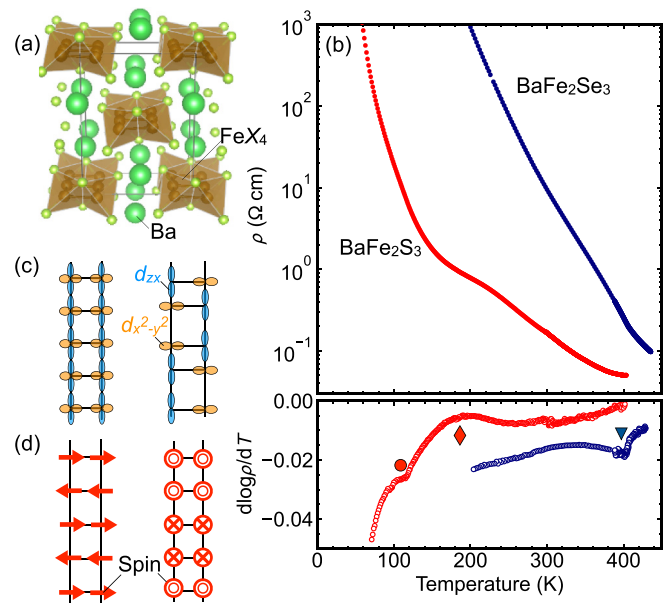


FIG. 1. (a) A schematic illustration of the crystal structure of BaFe_2X_3 with $Pnma$ space group depicted by VESTA [14]. (b) Temperature dependencies of electrical resistivity (ρ) and its temperature (T) derivative ($d \log \rho / dT$) for BaFe_2S_3 and BaFe_2Se_3 at ambient pressure. The data in (b) are taken from Ref. [15]. Schematic illustrations of (c) orbital and (d) magnetic order.

*aoyama@tohoku.ac.jp

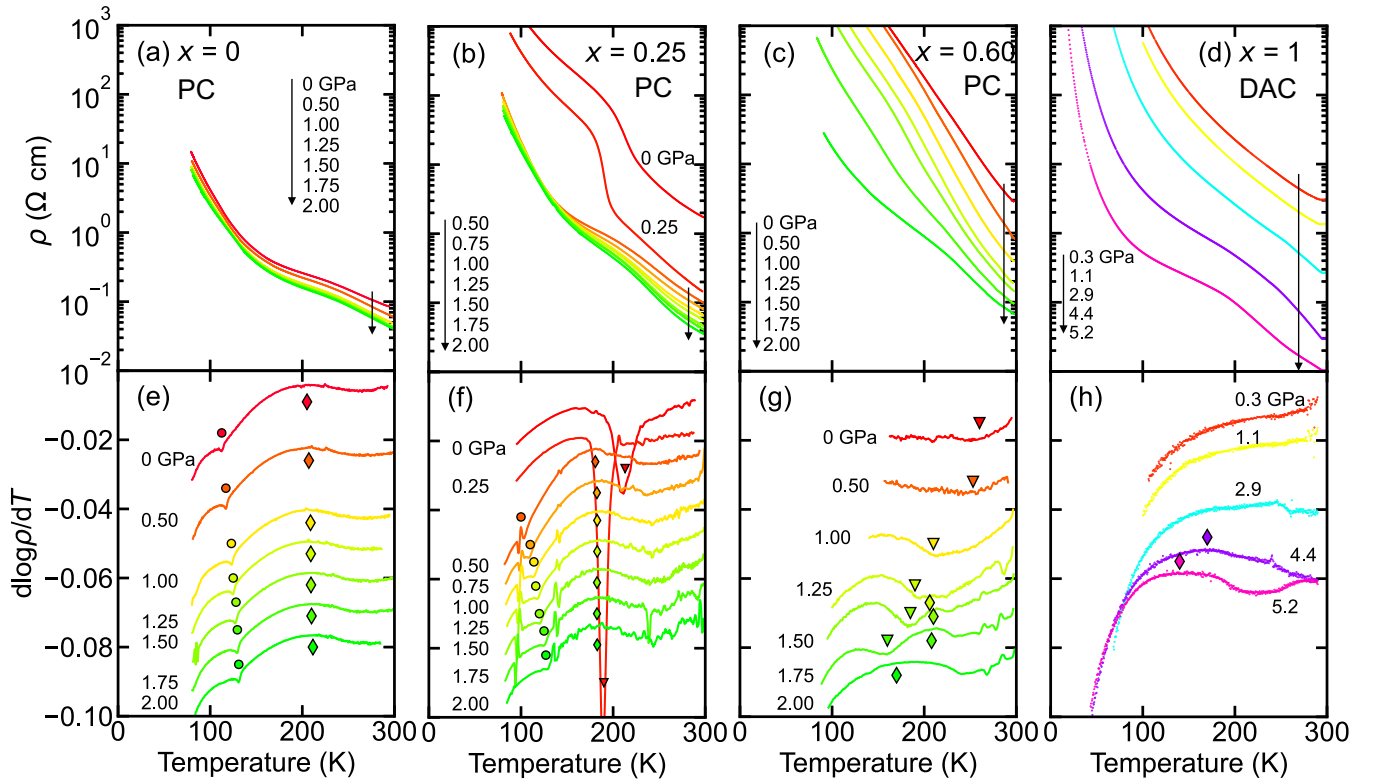


FIG. 2. Temperature dependencies of electrical resistivity (ρ) and its temperature (T) derivative ($d \log \rho/dT$) at various pressures of $\text{BaFe}_2(\text{S}_{1-x}\text{Se}_x)_3$ for (a), (e) $x = 0$, (b), (f) $x = 0.25$, (c), (g) $x = 0.60$, and (d), (h) $x = 1$. The $d \log \rho/dT$ are vertically shifted for clarity. The insets of (d) and (f) show the high-temperature parts of $d \log \rho/dT$. The ferroic and antiferro nematicity temperatures (T_F^* and T_{AF}^*) and Néel temperature (T_N) are indicated by diamonds, triangles, and circles, respectively. Results for $x = 1, 0.25$, and 0.60 were measured in the piston cylinder (PC) and $x = 1$ in the diamond anvil cell (DAC), respectively. See the main text for details.

account for a poor electrical conduction in the nematic phase. Thus, the electronic nematicity related to orbital ordering is well reflected in the electrical resistivity in the leg direction. Note that the nematicity referred to here is not identical to that of conventional two-dimensional iron-based superconductors. In the ladder system, the global fourfold rotational symmetry of the crystal structure is broken at higher temperatures before the formation of electronic nematicity. This contrasts with most iron-based superconductors, where fourfold rotational symmetry is broken by a nematic transition. Even though there are differences in electronic states below the nematic transition temperature, both have in common that the anisotropy changes due to antiferromagnetic and/or orbital ordering.

Consistent with the differences in electronic nematic states, BaFe_2S_3 and BaFe_2Se_3 differ in the magnetic order [Fig. 1(d)]. Stripe antiferromagnetism (AFM) is observed below $T_N = 115$ K in BaFe_2S_3 , whereas block AFM is observed below $T_N = 255$ K in BaFe_2Se_3 [16,27,28]. Block AFM is the exotic magnetic order in an orbital-selective Mott state [29–32]. The stripe AFM in BaFe_2S_3 induces a dipole anomaly in the differential electrical resistivity [circle in Fig. 1(b)], while the block AFM in BaFe_2Se_3 has a negligible impact on the electrical resistivity. Owing to the low-dimensional nature of the spin system, the nematic and magnetic ordering temperatures are well separated, which is a unique feature of iron-based ladder materials compared with iron-based superconductors in a two-dimensional square lattice.

Electronic nematicity has also been investigated in a solid solution, $\text{BaFe}_2(\text{S}_{1-x}\text{Se}_x)_3$ [15], which exhibits switching from ferroic to antiferro nematicity. Controlling the anion S/Se ratio involves an equivalence substitution, which enables bandwidth control by employing the chemical pressure effect [33,34]. Similar to chemical pressure, physical pressure may be an effective approach for controlling the electronic nematicity.

In this paper, we investigate the pressure evolution of nematicity in $\text{BaFe}_2(\text{S}_{1-x}\text{Se}_x)_3$ ($x = 0, 0.25, 0.60$, and 1) by examining the electrical resistivity measurement under various physical pressures. As a result, we reveal that the antiferro nematicity at $x = 0.25, 0.60$, and 1 switches to ferroic nematicity with the application of pressure. The critical pressure increases with increasing x . We discuss the electronic phase diagram in the temperature-pressure plane.

II. EXPERIMENT

Single crystals of $\text{BaFe}_2(\text{S}_{1-x}\text{Se}_x)_3$ were prepared using a slow cooling method with Ba (Sigma-Aldrich, 4N), Fe (Rare Metallic, 4N), S (Rare Metallic, 5N), and Se (Rare Metallic, 4N) as the starting materials. The mixture was placed in a carbon crucible and sealed in an evacuated quartz tube. Then, the quartz tube was heated in a furnace. The temperature was raised to 1100–1150 °C from room temperature over 5 h, held for 24 h, and then cooled down to 750 °C for 24–70 h. A piston cylinder cell (PC), a diamond anvil cell (DAC), and a

cubic anvil cell (CAC) were employed to measure the electrical resistivity (ρ) under high pressure (P). Glycerol and polyimide were used as the pressure media for the PC and CAC, and DAC, respectively. The pressure was determined for the PC, CAC, and DAC using load-pressure curves calibrated from the ruby fluorescence, the structural phase transitions of the standard sample measurements, and the *in situ* ruby fluorescence method at room temperature, respectively.

III. RESULTS AND DISCUSSION

Figure 2 shows the temperature (T) dependence of the electrical resistivity and $d \log \rho / dT$ for $x = 0, 0.25, 0.60$, and 1. In all data, the temperature profile is distinct from that of a single-gap insulator, which is closely associated with the orbital and magnetic order. For $x = 0$, a broad shoulder of ρ at ambient pressure is formed at $T_F^* = 205$ K, which is attributed to ferroic nematicity [Fig. 2(a)]. The detailed pressure variation can be tracked from $d \log \rho / dT$, shown in Fig. 2(e). The T_F^* value, which is characterized by a broad peak of $d \log \rho / dT$ (diamonds), shows a slight increase with increasing pressure, whereas the T_N value, which is characterized by a small dip structure (circles), significantly shifts to a higher temperature. The determination of the transition temperatures is in accordance with Yamauchi *et al.* [20]. These changes are summarized in the temperature-pressure phase diagram shown in Fig. 5(a).

For $x = 0.25$, a sharp increase in ρ with decreasing T is observed at $T_{AF}^* = 210$ K and 0 GPa, and at $T_{AF}^* = 190$ K and 0.25 GPa [triangles in Fig. 2(f)]. This is attributed to antiferroic nematicity. Increasing the pressure up to 0.5 GPa results in a drastic change; the electrical resistivity does not show a sudden increase at any temperature. Instead, it shows a characteristic temperature dependence similar to that observed for $x = 0$, indicating the stabilized ferroic nematicity at $T_{AF}^* = 180$ K shown by diamonds. Furthermore, a diplike anomaly in $d \log \rho / dT$ is observed at $T_N = 100$ – 130 K for pressures above 0.5 GPa [Fig. 2(f)], as observed for $x = 0$, suggesting the formation of the stripe-type antiferromagnetic order [35]. The results are summarized in a temperature-pressure phase diagram, as shown in Fig. 5(b). Notably, the antiferroic nematicity and block AFM are destabilized by pressure, and they switch to ferroic nematicity and stripe AFM at 0.5 GPa. The simultaneous switching in both orbital and spin channels indicates a close correlation between the two degrees of freedom. In high-pressure regions, T_N and T_F^* increase monotonically with increasing pressure, and T_N increases faster than T_F^* .

For $x = 0.60$, antiferroic nematicity occurs around $T_{AF}^* = 260$ K and ambient pressure. Similar to $x = 0.25$, antiferroic nematicity is destabilized by the applied pressure, and ferroic nematicity develops below $T_F^* = 206$ K at 1.25 GPa [Figs. 2(c) and 2(g)]. At 1.50–1.75 GPa, the two anomalies characterizing antiferroic and ferroic nematicity are observed in $d \log \rho / dT$, indicating a successive transition. At 2.0 GPa, the broad peak structure in the resistivity becomes much clearer, indicating the dominant ferroic nematicity [Fig. 2(c)]. A remarkable difference compared with $x = 0.25$ is that no diplike anomaly due to the magnetic order is observed in ferroic nematicity. However, we believe that the stripelike magnetism persists at this pressure regime, as discussed later.

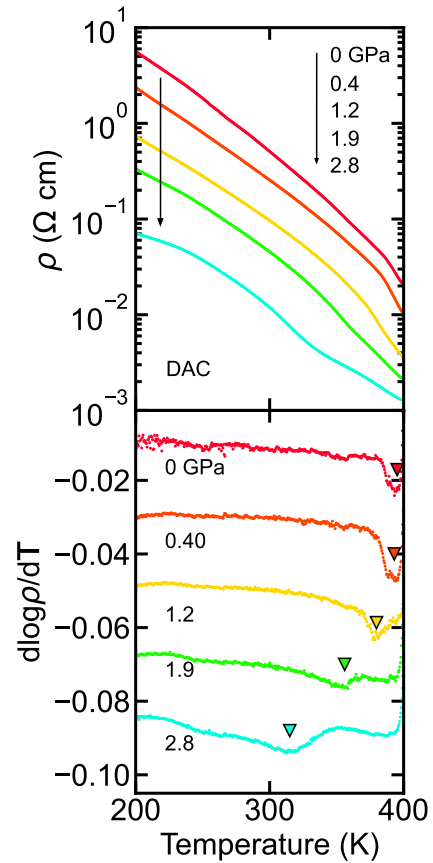


FIG. 3. Temperature (T) dependencies of electrical resistivity (ρ) and its temperature derivative of $x = 1$ for $\text{BaFe}_2(\text{S}_{1-x}\text{Se}_x)_3$.

For $x = 1$, the pressure dependence of electrical resistivity collected by using a diamond-type anvil cell is shown in Figs. 2(d), 2(h), and 3. Figures 2(d) and 2(h) cover $0 < T < 300$ K, and Fig. 3 covers $200 \text{ K} < T < 400$ K. In the measurement close to 0 GPa, a steep increase in electrical resistivity and a dip in $d \log \rho / dT$ due to antiferroic nematicity were observed at 400 K, which well reproduces the measurement under ambient pressure. With applying pressure, antiferroic nematicity is gradually suppressed, and T_{AF}^* reaches 316 K at 2.8 GPa (triangles in Fig. 3). A distinct shoulder in ρ is observed at pressures above 4.4 GPa, which is similar to the behavior observed for $x = 0$ [Fig. 2(d)]. Following $x = 0$, we define the maximum value of $d \log \rho / dT$ as T_{AF}^* . We conclude that the switching from antiferroic nematicity to ferroic nematicity occurs at around 4.4 GPa. As in the case of $x = 0.60$, no diplike anomaly due to antiferromagnetic order is observed in ferroic nematicity.

To examine the temperature dependence of resistivity for $x = 1$ under a quasihydrostatic pressure condition, we used a cubic anvil-type pressure apparatus, which can apply an isotropic pressure even after solidification of a liquid pressure medium, owing to its multianvil geometry. Figure 4 shows the pressure evolution of the resistivity as a function of temperature for $x = 1$. As observed in the DAC measurement, the steep divergence of resistivity is suppressed at around 200 K in 5.7 GPa, and the temperature dependence becomes similar to that in BaFe_2S_3 . This is consistent with the stabilized ferroic nematicity at around 4 GPa. Therefore, the

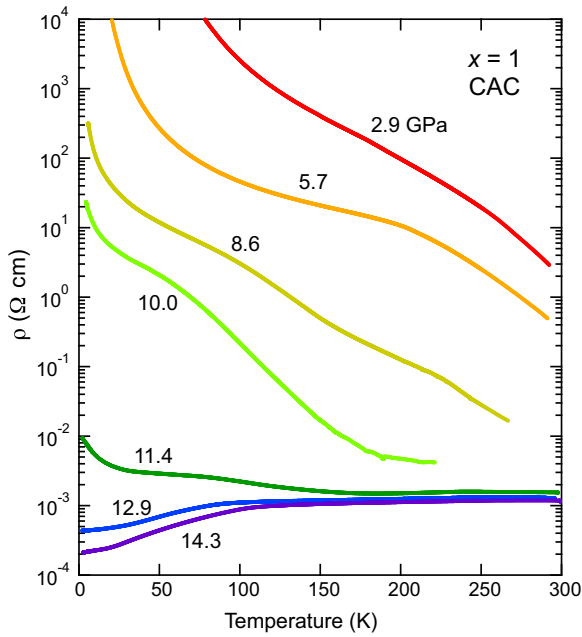


FIG. 4. Temperature dependence of electrical resistivity (ρ) of $x = 1$ for $\text{BaFe}_2(\text{S}_{1-x}\text{Se}_x)_3$ under high pressure measured using a cubic anvil cell (CAC).

switching behavior is observed in both the DAC and CAC measurements, indicating that this phenomenon is robust to the pressure condition. With increasing pressure, the Mott gap is gradually suppressed, and an insulator-metal transition

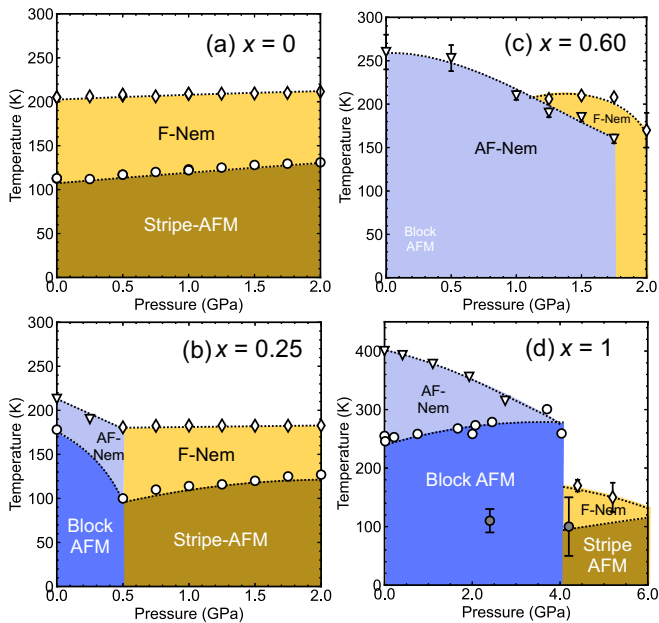


FIG. 5. Electronic phase diagram in the temperature-pressure plane for $\text{BaFe}_2(\text{S}_{1-x}\text{Se}_x)_3$, (a) $x = 0$, (b) $x = 0.25$, (c) $x = 0.60$, and (d) $x = 1$. The transition temperatures are determined by analyzing the data collected using PC for $x = 0, 0.25$, and 0.60 , and DAC for $x = 1.0$. The T_F^* and T_{AF}^* represent the transition temperatures of ferroic nematicity (F-Nem) and antiferroic nematicity (AF-Nem), respectively. The T_N is the antiferromagnetic transition temperature. The antiferromagnetic transition in (d) is based on literature values; white circles are from Ref. [37] and gray circles are from Ref. [38].

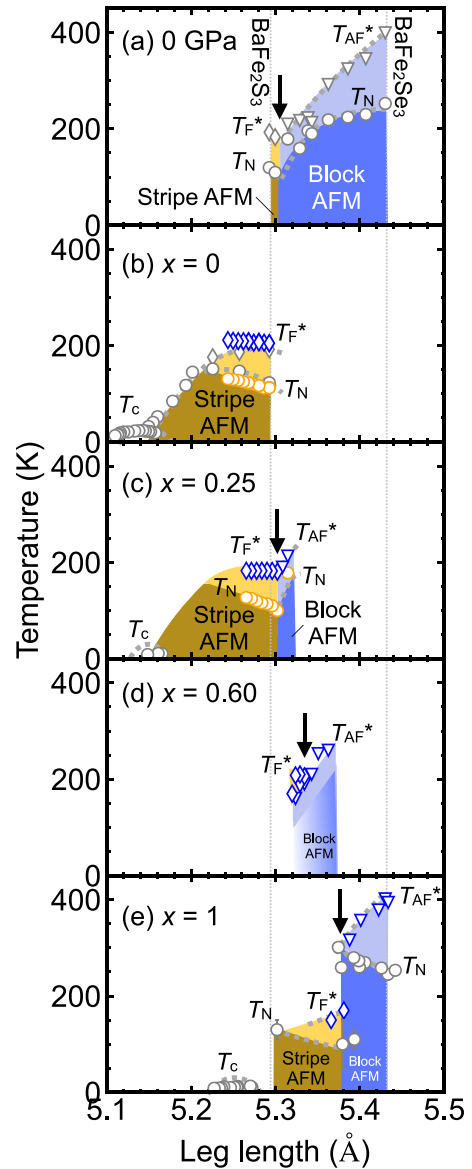


FIG. 6. Electronic phase diagrams obtained as a function of the lattice constant at room temperature along the leg direction for the (a) x dependence of $\text{BaFe}_2(\text{S}_{1-x}\text{Se}_x)_3$ and pressure dependencies of (b) $x = 0$, (c) 0.25 , (d) 0.60 , and (e) 1 . The antiferromagnetic (nematic) transitions are marked in orange (blue). The symbol types are in accordance with Fig. 1. Open gray circles are previously reported data taken from Refs. [15,17,20,36]. The vertical gray dotted lines at 5.29 and 5.43 Å indicate the leg length of BaFe_2S_3 and BaFe_2Se_3 . The black solid arrows correspond to the nematicity switching.

occurs at around 12 GPa. The absence of a superconducting drop in the resistivity near the insulator-metal transition is in stark contrast to the DAC experiment reported in Refs. [17,36]. This suggests that anisotropic compression is necessary for the superconductivity in this material.

All the phase transition temperatures collected in DAC of $x = 1$ are summarized in Fig. 5(d). In addition to our results, T_N determined by two other neutron diffraction groups are also plotted [37,38]. Note that the measurements obtained by the two groups show a discrepancy in T_N although both groups

observed that the block magnetism collapses at approximately 4 GPa. By comparing the temperature–pressure phase diagram for all compositions, the several anomalies in ρ caused by the magnetic and nematic transitions are commonly observed over a wide range of compositions and pressures, indicating that a comprehensive electronic phase diagram can be obtained by considering the appropriate parameters. Figure 6 shows plots of the T_F^* , T_{AF}^* , T_N , and T_c for $x = 0, 0.25, 0.60$, and 1 as functions of the lattice constant along the leg direction, where T_c is the superconducting transition temperature reported in Refs. [16,17,36]. Note that the lattice constants under high pressure have not been reported for $x = 0.25$ and 0.60, hence, the lattice constants were estimated from a relationship $\frac{d\ell}{\ell} = -\beta dP$ (ℓ being the lattice constant, and β being the compressibility), where we used the interpolated β value for $x = 0.25$ and 0.60.

The global phase diagram shown in Fig. 6 can be summarized as follows. When the leg length is long, the antiferroic nematicity/block AFM is stable in the Mott insulating state. With decreasing leg length, the nematic/spin orders switch to ferroic nematicity/stripe AFM. When the leg length decreases further, a metal-insulator transition and superconducting transition occur next to the ferronematic/stripe AFM phase. Because the leg length is correlated with the transfer integral along the leg direction, it is reasonable to assume that the electronic phase diagram is dominated by the one-electron bandwidth W along the leg direction.

This hypothesis is supported by several theoretical studies that analyzed the effective model for iron-based ladder materials [39–42]. These theories indicate that the ground state magnetic structure changes from the block AFM to paramagnetism via the stripe AFM as one increases the bandwidth. Even though these theoretical studies do not mention electronic nematicity, if one supposes a one-to-one correspondence between ferroic nematicity/stripe AFM and antiferroic nematicity/block AFM, the observed electronic phase diagram is well interpreted. The fact that antiferroic nematicity with high resistivity is more stable than ferroic nematicity with low resistivity in the small bandwidth regime is in harmony with our physical intuition.

Finally, let us consider the characteristics of the individual phase diagrams. At first, we compare Figs. 6(a)–6(c). The leg length dependencies of T_F^* and T_N in Figs. 6(a) and 6(b) are systematically connected. In Figs. 6(a) and 6(c), the switch in nematicity (indicated by the black arrows) occurs for

approximately the same leg length. Furthermore, T_F^* , T_N , and T_c in Figs. 6(b) and 6(c) have an almost identical dependence on leg length. Therefore, the chemical and physical pressures for small x values have an equivalent effect on the bandwidth control. Next, we move to the phase diagrams for $x = 0.60$ and 1.0, shown in Figs. 6(d) and 6(e). The pressure-induced switch in nematicity at $x = 0.60$ and 1.0 occurs at a longer leg length than that at $x = 0.25$, and the critical leg length gets longer as x increases. Furthermore, the Mott transition at $x = 1$ also occurs at a longer leg length than that at $x = 0$ and 0.25. This indicates that chemical and physical pressure works nonequivalently for larger x values. When the atomic number of the anion is larger, the physical pressure appears to work not only as a simple bandwidth control but also as a filling control by self-doping from anions to cations, thus efficiently suppressing the charge gap. The smaller electronegativity of selenium compared with that of sulfur supports this interpretation.

IV. SUMMARY

In summary, we have systematically investigated the electrical resistivity of $\text{BaFe}_2(\text{S}_{1-x}\text{Se}_x)_3$ under various applied pressures. As a result, we have clarified that the antiferroic nematicity at $0.25 \leq x \leq 1$ switches to ferroic nematicity by the application of pressure. From the results, we have constructed the electronic phase diagram with respect to the lattice parameter along the leg direction. Based on the electronic phase diagram, we have discussed the relationship between nematicity switching and bandwidth. We also discussed that in Se-rich compositions, the external pressure causes a filling control by an effective charge transfer.

ACKNOWLEDGMENTS

This work is financially supported by JSPS KAKENHI Grants No. JP22H01175, No. JP22K18680, No. JP22H00102, No. JP19H05823, No. JP19H05822, No. JP19K21837, No. JP18H01159, No. JP16H04019, No. JP16H01062, No. JP18H04302, No. JP18K03531, No. JP16K17732, No. JP20K14396, No. JP17H05474, No. JP19H04685, No. JP17K05531, No. JP20K03830, and No. JP20H02604; by Murata Science Foundation; and by JST CREST under Grant No. JP19198318.

[1] C.-C. Lee, W.-G. Yin, and W. Ku, *Phys. Rev. Lett.* **103**, 267001 (2009).
 [2] W. Lv, J. Wu, and P. Phillips, *Phys. Rev. B* **80**, 224506 (2009).
 [3] C.-C. Chen, J. Maciejko, A. P. Sorini, B. Moritz, R. R. P. Singh, and T. P. Devereaux, *Phys. Rev. B* **82**, 100504(R) (2010).
 [4] C. Fang, H. Yao, W.-F. Tsai, J. P. Hu, and S. A. Kivelson, *Phys. Rev. B* **77**, 224509 (2008).
 [5] C. Xu, M. Müller, and S. Sachdev, *Phys. Rev. B* **78**, 020501(R) (2008).
 [6] R. M. Fernandes, L. H. VanBebber, S. Bhattacharya, P. Chandra, V. Keppens, D. Mandrus, M. A. McGuire, B. C. Sales,

A. S. Sefat, and J. Schmalian, *Phys. Rev. Lett.* **105**, 157003 (2010).
 [7] H. Kontani and S. Onari, *Phys. Rev. Lett.* **104**, 157001 (2010).
 [8] S. Onari and H. Kontani, *Phys. Rev. Lett.* **109**, 137001 (2012).
 [9] S. Kasahara, H. J. Shi, K. Hashimoto, S. Tonegawa, Y. Mizukami, T. Shibauchi, K. Sugimoto, T. Fukuda, T. Terashima, A. H. Nevidomskyy, and Y. Matsuda, *Nature (London)* **486**, 382 (2012).
 [10] K. Nakayama, Y. Miyata, G. N. Phan, T. Sato, Y. Tanabe, T. Urata, K. Tanigaki, and T. Takahashi, *Phys. Rev. Lett.* **113**, 237001 (2014).

- [11] S. A. Kivelson, E. Fradkin, and V. J. Emery, *Nature (London)* **393**, 550 (1998).
- [12] E. Fradkin, S. A. Kivelson, M. J. Lawler, J. P. Eisenstein, and A. P. Mackenzie, *Annu. Rev. Condens. Matter Phys.* **1**, 153 (2010).
- [13] R. M. Fernandes, A. V. Chubukov, and J. Schmalian, *Nat. Phys.* **10**, 97 (2014).
- [14] K. Momma and F. Izumi, *J. Appl. Crystallogr.* **44**, 1272 (2011).
- [15] S. Imaizumi, T. Aoyama, R. Kimura, K. Sasaki, Y. Nambu, M. Avdeev, Y. Hirata, Y. Ikemoto, T. Moriwaki, Y. Imai, and K. Ohgushi, *Phys. Rev. B* **102**, 035104 (2020).
- [16] H. Takahashi, A. Sugimoto, Y. Nambu, T. Yamauchi, Y. Hirata, T. Kawakami, M. Avdeev, K. Matsubayashi, F. Du, C. Kawashima, H. Soeda, S. Nakano, Y. Uwatoko, Y. Ueda, T. J. Sato, and K. Ohgushi, *Nat. Mater.* **14**, 1008 (2015).
- [17] J. Ying, H. Lei, C. Petrovic, Y. Xiao, and V. V. Struzhkin, *Phys. Rev. B* **95**, 241109(R) (2017).
- [18] L. Zheng, B. A. Frandsen, C. Wu, M. Yi, S. Wu, Q. Huang, E. Bourret-Courchesne, G. Simutis, R. Khasanov, D. X. Yao, M. Wang, and R. J. Birgeneau, *Phys. Rev. B* **98**, 180402(R) (2018).
- [19] P. Materne, W. Bi, J. Zhao, M. Y. Hu, M. L. Amigó, S. Seiro, S. Aswartham, B. Büchner, and E. E. Alp, *Phys. Rev. B* **99**, 020505(R) (2019).
- [20] T. Yamauchi, Y. Hirata, Y. Ueda, and K. Ohgushi, *Phys. Rev. Lett.* **115**, 246402 (2015).
- [21] K. Takubo, Y. Yokoyama, H. Wadati, S. Iwasaki, T. Mizokawa, T. Boyko, R. Sutarto, F. He, K. Hashizume, S. Imaizumi, T. Aoyama, Y. Imai, and K. Ohgushi, *Phys. Rev. B* **96**, 115157 (2017).
- [22] T. Aoyama, S. Imaizumi, T. Togashi, Y. Sato, K. Hashizume, Y. Nambu, Y. Hirata, M. Matsubara, and K. Ohgushi, *Phys. Rev. B* **99**, 241109(R) (2019).
- [23] V. Svitlyk, D. Chernyshov, E. Pomjakushina, A. Krzton-Maziopa, K. Conder, V. Pomjakushin, R. Pöttgen, and V. Dmitriev, *J. Phys.: Condens. Matter* **25**, 315403 (2013).
- [24] S. Hosoi, T. Aoyama, K. Ishida, Y. Mizukami, K. Hashizume, S. Imaizumi, Y. Imai, K. Ohgushi, Y. Nambu, M. Kimata, S. Kimura, and T. Shibauchi, *Phys. Rev. Res.* **2**, 043293 (2020).
- [25] R. Arita, H. Ikeda, S. Sakai, and M.-T. Suzuki, *Phys. Rev. B* **92**, 054515 (2015).
- [26] M.-T. Suzuki, R. Arita, and H. Ikeda, *Phys. Rev. B* **92**, 085116 (2015).
- [27] J. M. Caron, J. R. Neilson, D. C. Miller, A. Llobet, and T. M. McQueen, *Phys. Rev. B* **84**, 180409(R) (2011).
- [28] Y. Nambu, K. Ohgushi, S. Suzuki, F. Du, M. Avdeev, Y. Uwatoko, K. Munakata, H. Fukazawa, S. Chi, Y. Ueda, and T. J. Sato, *Phys. Rev. B* **85**, 064413 (2012).
- [29] M. Mourigal, S. Wu, M. B. Stone, J. R. Neilson, J. M. Caron, T. M. McQueen, and C. L. Broholm, *Phys. Rev. Lett.* **115**, 047401 (2015).
- [30] J. Herbrych, N. Kaushal, A. Nocera, G. Alvarez, A. Moreo, and E. Dagotto, *Nat. Commun.* **9**, 3736 (2018).
- [31] J. Herbrych, J. Heverhagen, N. D. Patel, G. Alvarez, M. Daghofer, A. Moreo, and E. Dagotto, *Phys. Rev. Lett.* **123**, 027203 (2019).
- [32] N. D. Patel, A. Nocera, G. Alvarez, A. Moreo, S. Johnston, and E. Dagotto, *Commun. Phys.* **2**, 64 (2019).
- [33] J. Yu, M. Wang, B. A. Frandsen, H. Sun, J. Yin, Z. Liu, S. Wu, M. Yi, Z. Zhu, A. Acharya, Q. Huang, E. Bourret-Courchesne, J. W. Lynn, and R. J. Birgeneau, *Phys. Rev. B* **101**, 235134 (2020).
- [34] Y. J. Fan, J. Y. Liu, J. J. Feng, Z. C. Chen, M. H. Wang, Z. He, H. T. Guo, B. Qian, Z. X. Shi, and W. Zhou, *Supercond. Sci. Technol.* **35**, 085007 (2022).
- [35] The anomalies at 100 and 140 K are due to artifacts.
- [36] H. Takahashi, R. Kikuchi, C. Kawashima, S. Imaizumi, T. Aoyama, and K. Ohgushi, *Materials* **15**, 1401 (2022).
- [37] S. Wu, J. Yin, T. Smart, A. Acharya, C. L. Bull, N. P. Funnell, T. R. Forrest, G. Simutis, R. Khasanov, S. K. Lewin, M. Wang, B. A. Frandsen, R. Jeanloz, and R. J. Birgeneau, *Phys. Rev. B* **100**, 214511 (2019).
- [38] W.-G. Zheng, V. Balédent, C. V. Colin, F. Damay, J.-P. Rueff, A. Forget, D. Colson, and P. Foury-Leylekian, *Commun. Phys.* **5**, 183 (2022).
- [39] Q. Luo, A. Nicholson, J. Rincón, S. Liang, J. Riera, G. Alvarez, L. Wang, W. Ku, G. D. Samolyuk, A. Moreo, and E. Dagotto, *Phys. Rev. B* **87**, 024404 (2013).
- [40] Y. Zhang, L. Lin, J. J. Zhang, E. Dagotto, and S. Dong, *Phys. Rev. B* **95**, 115154 (2017).
- [41] Y. Zhang, L.-F. Lin, J.-J. Zhang, E. Dagotto, and S. Dong, *Phys. Rev. B* **97**, 045119 (2018).
- [42] Z. Liu, X.-S. Ni, L. Li, H. Sun, F. Liang, B. A. Frandsen, A. D. Christianson, C. dela Cruz, Z. Xu, D.-X. Yao, J. W. Lynn, R. J. Birgeneau, K. Cao, and M. Wang, *Phys. Rev. B* **105**, 214303 (2022).